Available online at www.eccomasproceedia.org
Eccomas Proceedia SMART (2023) 1808-1816

ECCOMAS
Proceedia

X ECCOMAS Thematic Conference on Smart Structures and Materials
SMART 2023
D.A. Saravanos, A. Benjeddou, N. Chrysochoidis and T. Theodosiou (Eds)

NONLINEAR FINITE ELEMENT FORMULATION OF RAM MEMORIES BASED ON PHASE–CHANGE THERMOELECTRICS

JOSÉ L. PÉREZ-APARICIO*, ROBERTO PALMA†

*Continuum Mechanics and Theory of Structures
Universitat Politècnica de València
Camino de Vera s/n, 46011 Valencia, Spain
e-mail: jopeap@mes.upv.es

†Structural Mechanics and Hydraulic Engineering
University of Granada
Campus Fuentenueva, 18071 Granada, Spain
e-mail: rpalgue@ugr.es

Abstract. The current work presents a nonlinear and displacement–based finite element formulation to study the temperature and electric voltage distributions and mechanical stresses of non–volatile computer memories based on phase–change of thermoelectric materials. The main advantage of volatile memories is their reduced energy consumption and ability to work without a power supply since they store energy by the phase–change from amorphous to crystalline. However, the high temperature producing this phase–change can cause electric and mechanical failure. Numerically, the model presents two difficulties: i) two nonlinearities due to the Joule heating, which quadratically depends on the electric field and the temperature dependency of the material properties, and ii) discontinuities in the physical magnitudes when the phase–change is achieved. The first difficulty is solved using the Newton–Raphson algorithm, and the second by introducing a regularization parameter. Finally, two designs from the literature are numerically simulated to analyze the distributions before and after the phase–change. The T–shape is the worst design since it requires a higher temperature to change the phase, and this increase results in mechanical failure.

Key words: Thermoelectric, Finite Element, Phase–change, Random Access Memory, Mechanical stress

1 INTRODUCTION

In the coming decades, the technology that will define and shape the economy and society will be computing. However, calculations face a severe efficiency problem since most algorithms run on conventional systems, such as Central Processing Units, Data Processing Units, Graphical Processing, and Field Programmable Gate Arrays.

Peer-review under responsibility of the organizing committee of SMART 2023.
doi: 10.7712/150123.9951.451159

As argued in [1], to mitigate this problem, a transition to architectures with better–located memory and processing is needed. In this context, electronic memories based on phase–change Materials PCM—also known as non–volatile memories—are based on the difference in electrical resistivity phases of the materials. The most common PCM memories are made out of GST ($GeSbTe$, germanium–antimony–tellurium), which can have different geometrical configurations and operate in two distinct phases:

- The RESET phase refers to the amorphous (with high resistivity) state of the material created by applying electrical pulses.
- The SET phase refers to the crystalline (with low resistivity) state created by increasing the temperature T above the crystallization of the amorphous phase.

In practice, PCM memories have the advantage of storing data without a power supply, thus preventing data from being lost during a power interruption. In addition, among its many other benefits compared to volatile memories, it is worth highlighting its higher performance, greater storage capacity, and lower power consumption. However, as they are novel storage systems, PCM memories require in–depth study.

The most significant disadvantage of PCM memories lies in their small dimensions, needing high electrical currents and high ΔT and producing thermo–electro–mechanical failures.

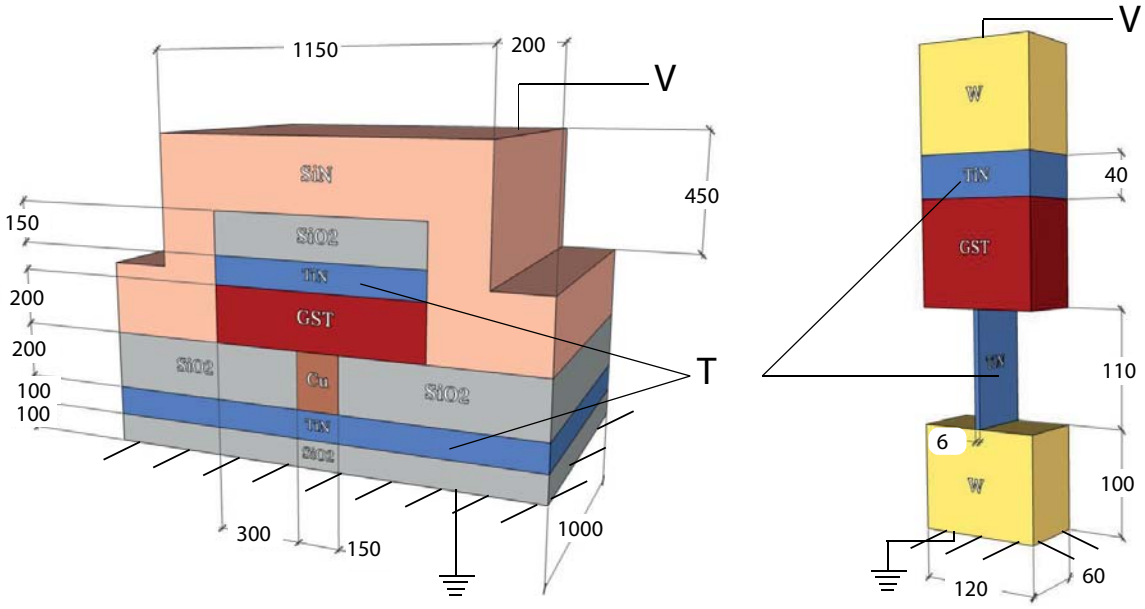

Figure 1: `T`–shaped (left) and `Knive` (right) geometries for phase–change material devices. Dimensions in nm. Lower faces are mechanically clamped and electrically grounded to zero.

Analytically, [1] investigated the critical (for miniaturization) Thomson thermoelectric TE effect. The resulting asymmetric positioning of the amorphous zone during RESET makes the

PCM operation depend on the anode contact configuration. Line cells with PCM extensions over the contact area perform better since lower RESET currents and SET threshold voltages V (through the Joule effect) are necessary, and the cell is more robust against over–programming faults.

The research of [2] focuses on obtaining high efficiency by optimizing the materials' design so that the TE effect gets most of the heat generated during the operation of PCM devices. Another objective was to achieve a very low RESET operating current: they carried out different simulations considering the Peltier effect and the bias current and V decrease; consequently, the total power consumption also decreased. It was further found that the results could be improved by changing the TiN to n–type doped Si. This improvement raised the possibility of a nanodevice of ultra–low power. It was also found that using n–type Si required significantly less current than p–type Si to convert the GST material to the amorphous state. After all these tests, it was shown that the Peltier effect plays a crucial role in reducing the RESET electric intensity.

In the context of solutions based on the Finite Element Method FEM, in [3], the commercial program COMSOL simulates processes during the RESET phase. After contrasting experimental observations and simulations on a p–type PCM, it was observed that there was a similar degree of asymmetry in the T profiles in two cases since the hottest spot in the cell tended to move toward the end of higher V. Both results confirm that asymmetries in PCM devices are due to TE phenomena.

The previous reference extended their work in [4] and [3] to include the Thomson effect and different geometries: T– and W–type (wedge). They concluded that the Thomson effect caused the asymmetries through the several material connections and, in addition, it was shown that for both geometries, there is an electric flux preferential direction that leads to lower energy consumption during the RESET phase and at smaller T gradients, which turns out to be beneficial in terms of reducing element segregation and device failure.

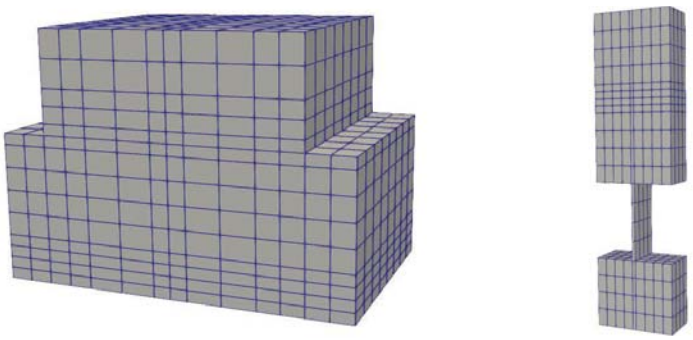

Figure 2: Finite Element meshes for `T`–shaped (left) and `Knive` (right) geometries.

Another model based on the FEM is [5]. A 3D simulation studied T–distributions in the PCM cells to understand the switching between SET and RESET. In addition to the Thomson effect,

other TE effects, such as Peltier and Seebeck, were investigated. According to the authors, more research is needed to develop PCM cells with higher thermal efficiency, and the cooling rate determines the final phase distribution. Finally, both switching operations occur mainly from the melting and rapid cooling of the PCM near the contact between the lower electrode and the PCM.

A recent publication [6] emphasized the need to use resistive memory devices for in–memory computing, with a comprehensive review of the most advanced PCM state–of–the–art.

For the geometries of the present work, it is observed that the most significant difference between considering the Thomson effect happens in the V–distributions since this effect is related to the Seebeck coefficient that couples V and T gradients. The following results are for an electric intensity that changes the phase– change. Sometimes the GST is subjected to a much higher T so that the material not only crystalizes but also partially melts, with a much intense but shorter electric pulse. Some geometries that confine the GST do not allow this substantial increase since all materials would melt.

This intensity is numerically calculated so that in the GST, $T \approx 170$°C at some points, a 15% increase above T_{cr}, [7]; the values are 10.25 μA for the first geometry and 16 μA for the second (see Sections 3 and 4). In practice, these intensities are indirectly applied with a laser pulse, but numerically they are prescribed with an equivalent $\bar{V}$; see Figure 1. Both the top and bottom sides are prescribed to T = 50°.

2 FORMULATION

From [8], [9], and [10] and with the standard boundary conditions and notation, the complete TE formulation comprises the balance Eqs. (1) and constitutive Eqs. (2) equations for the Mechanical, Thermal, and Electric fields. In indicial notation:

$$\begin{cases} \rho\ddot{u}_i & = \sigma_{ij,j} + f_i \\ \rho c_p \dot{T} & = -q_{i,i} + Q + j_i E_i + \alpha_{_T} \delta_{ij} \dot{\epsilon}_{ij} - \rho L \dfrac{\partial}{\partial t} h(T - T_{cr}) \\ j_{i,i} & = 0 \end{cases} \tag{1}$$

$$\begin{cases} \sigma_{ij} & = C_{ijkl}\epsilon_{ij} - \alpha_{_T}\Delta T \delta_{ij} \\ q_i & = -\kappa T_{,j} + \alpha T j_i \\ j_i & = -\gamma V_{,j} - \alpha\gamma T_{,i} \end{cases} \tag{2}$$

where the supra dot ($\dot{}$) indicates derivative with respect to time t, u_i the displacement, σ_{ij} the stress, f_i the forces, q_i, j_i the heat and electric fluxes, Q the heat source, E_i the electric field, δ_{ij} the Kronecker delta, ϵ_{ij} the strain, C_{ijkl} the stiffness, and γ the electric conductivity. The rest of the symbols are defined in the following equations and in Table 1

The only addition to the standard mechanical–TE formulation comes from the phase of change, the last term in the second balance equation and the Debye term function of $\dot{\epsilon}_{ij}$. To

develop the first term, the entropy H and its balance must be expressed as:

$$H = \int_0^T \rho c_p \, \mathrm{d}T + \rho L \, h(T - T_{cr}) \; ; \qquad \dot{H} = -\nabla \cdot \mathbf{q} + Q \tag{3}$$

where $\mathbf{q}$ is the heat flux vector, T_{cr} the crystalization temperature. The Heaviside function $h(T - T_{cr})$ takes the value 0 for $T < T_{cr}$ and 1 for $T > T_{cr}$.

In the current work, the chosen FEM implementation is the Heat Source Method from [11]. From both Eqs. (3) and approximating the time derivative with an explicit time integration scheme:

$$\rho c_p \dot{T} = -\nabla \cdot \mathbf{q} + Q - \frac{\partial}{\partial t}\Big[\rho L \, h(T - T_{cr})\Big] \approx -\nabla \cdot \mathbf{q} + Q - \rho L \, \frac{h_{n+1} - h_n}{\Delta t} \tag{4}$$

where n and $n+1$ represent the current– and next–time steps. Multiplying this strong form by the test function δT, applying the Divergence theorem, and with the standard FEM discretizations of the type $T \approx N_a \mathbf{T}_a^\top$, the thermal residual in an element e and at a node a can be calculated with Eq. (5). In the previous expression, N_a is the matrix of shape function derivatives, and $\mathbf{T}_a$ the vector with the temperatures of all element nodes.

$$\begin{aligned} R_{a_{n+1}} = \; & \int_{\Omega_e} \Big[\mathbf{B}_{a_{n+1}}^\top \mathbf{q}_{n+1} \Delta t + N_{a_{n+1}} Q \Delta t - N_{a_{n+1}} \rho c_p \dot{T}_{n+1} \Delta t - N_{a_{n+1}} \rho L \, (h_{n+1} - h_n)\Big] \, \mathrm{d}\Omega_e \\ & + \int_{\Gamma_e} N_{a_{n+1}} \bar{q} \, \mathrm{d}\Gamma_e \end{aligned} \tag{5}$$

where $\bar{q} = q_i \; n_i$ is the prescribed perpendicular heat flux at the boundary. This residual is discontinuous due to the Heaviside function, which has to be regularized. For both steps n and $n+1$, with a small ϵ = 1.25:

$$h(T - T_{cr}) = \begin{cases} 0 & T \leq T_{cr} - \epsilon \\ \dfrac{T - (T_{cr} - \epsilon)}{2\epsilon} & T_{cr} - \epsilon \leq T \leq T_{cr} + \epsilon \\ 1 & T \geq T_{cr} + \epsilon \end{cases} \tag{6}$$

Concerning the usual TE formulation in the FEM, the new term of Eq. (5) representing the phase–change is a new heat source in the last term of the volumetric integral. Upon derivation with respect to $\mathbf{T}_{a_{n+1}}^\top$ and $\dot{\mathbf{T}}_{a_{n+1}}^\top$, the stiffness and capacity matrices are obatined.

3 `Knive` GEOMETRY

The `Knive` geometry and its dimensions are shown in Figure 1 right. The lower and upper layers of the cell are made out of Tungsten W electrodes, while the intermediate layers correspond to a GST–TiN interface. One of the TiN components is very thin, and the properties of all materials are listed in the Appendix.

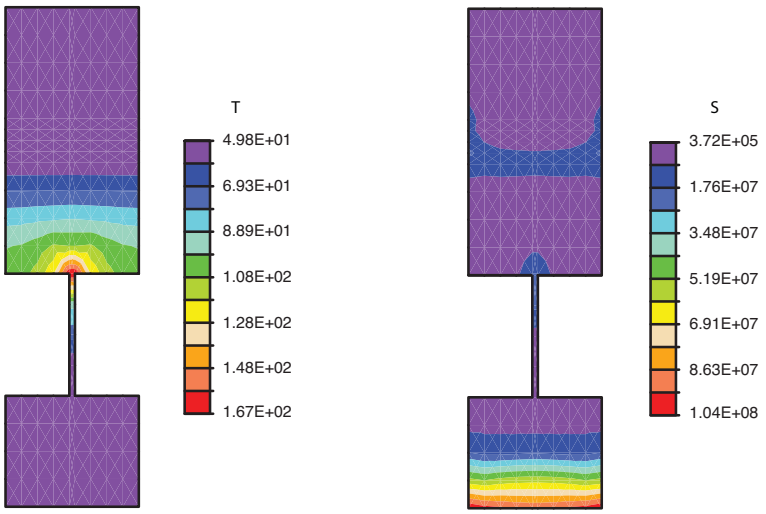

Figure 3: For `Knive` geometry, temperature °C (left) and Tresca stress in Pa (right).

Figure 2 right shows the FEM mesh with 592 3D eight–node elements (brick type) with 1250 nodes. Each node includes five degrees of freedom: three displacements, T, and V.

In the left and central figures, it is observed that the T and V essential boundary conditions at the top and bottom are fulfilled. There is a strong nonlinear distribution in the vertical direction, and there is not much variation in horizontal planes except when the area changes abruptly. Only some points of the GST have crystalized due to the sharp area transition between GST and TiN: in this sense, the geometrical design needs to be corrected.

Figure 3 right draws isolines for the Tresca equivalent stress. Although some materials are fragile and this equivalent stress could not be accurate, the same criteria have been used in the whole mesh to be consistent with the FEM smoothing. A moderate 104 MPa is calculated at the lower W base since the PCM is built in this area. Since the allowable tensile stress of this material is about 1100 MPa, no damage is predicted.

4 `T`–SHAPE GEOMETRY

Figure 2 left shows the geometry and dimensions of an inverted `T`–shaped memory cell. This model consists of a silicon nitride Si_3N_4 capping layer, a silicon dioxide SiO_2 hard mask, a GST/TiN PCM interface, a transversal Cu electrode contact surrounded by a SiO_2 barrier and a lower TiN electrode. Figure 4 shows the FEM mesh of 1408 3D elements and 3726 nodes, many more than those of the previous geometry.

The T–distribution of Figure 4 top left indicates that an important part of the GST is crystallizing with this geometry. In Figure 4 bottom, the maximum equivalent stress is 165 MPa in Cu, close to the GST; since the admissible value is about 220 MPa, there is the possibility of PCM misfunction if more intensity is applied.

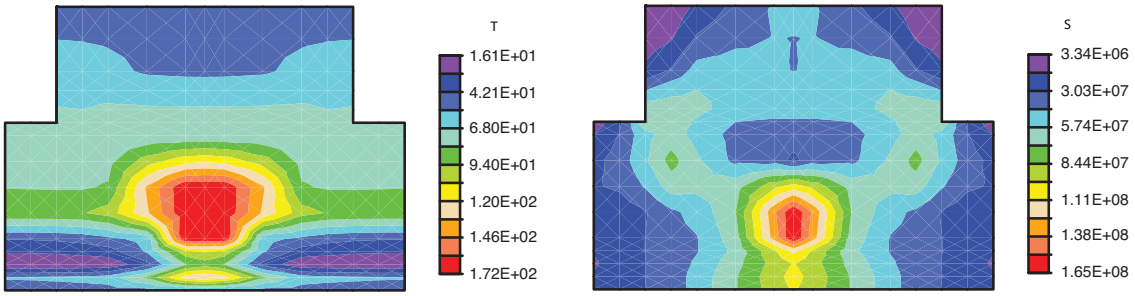

Figure 4: For T–shape geometry, temperature in °C (left top) and Tresca stress in Pa (bottom).

5 CONCLUSIONS

- The finite element code correctly solves the nonlinearity of Phase–Change Materials behavior, as shown in Figures 3 and 4.

- The T–shape is not a good design since the device would break during operation due to high mechanical stresses. In contrast, the Knive is a good mechanical design but the material only changes phase progressively with the application of current.

- In future works, the present numerical tool could be used to design and optimize the PCMs dimensions and geometries, different from those of the present work.

6 APPENDIX

Property	Name	Unit	W	TiN	GST	SiO_2	Cu	Si_3N_4
$E \times 10^9$	Young modulus	Pa	400	41.6	$(7)_1$	66.3	124	232
ν	Poisson coeff.	–	0.28	0.33	0.3	0.19	0.34	0.25
$\alpha_T \times 10^{-6}$	Thermal exp.	1/K	4.4	5.4	$(7)_2$	0.75	17	2.55
$\rho_{el} \times 10^{-8}$	Electr. resistivity	Ω·m	5.71	$(8)_1$	$(8)_1$	640×10^8	1.69	720
κ	Thermal conduc.	W/m·K	178	$(8)_2$	$(8)_2$	1.5	386	27
$\rho \times 10^3$	Density	kg/m^3	19.3	5.4	6.2	2.65	8.96	3.21
c_p	Heat capacity	J/kg·K	132	784	202	730	390	760
α	Seebeck coeff.	V/K	0	$(8)_3$	$(8)_3$	0	0	0
L	Latent heat	J/kg	0	0	$(8)_4$	0	0	0

Table 1: Material properties from [7] and [3]. From Eqs. (7), discontinuous properties due to phase–change; from Eqs. (8), T–variable properties.

For GST, Young's modulus and thermal expansion coefficient are linear and different in the

two phases, with a jump at T = 150°C:

$$\begin{array}{ll} T \leq 150^{\circ}\mathrm{C} & T \geq 150^{\circ}\mathrm{C} \\ E = 18 + 0.012\,T\ ; & E = 38 + 0.0133\,T \\ \alpha_{_T} = \big(1 + 0.02\,T\big)\times 10^3\ ; & \alpha_{_T} = \big(6 - 0.01133\,T\big)\times 10^3 \end{array} \tag{7}$$

For two materials, several properties are a function of T; in °C the expressions are:

$$\begin{array}{ll} TiN & GST \\ \rho_{el} = 2.034 + 1.4\times 10^{-3}\,T - 1.6\times 10^{-6}\,T^2\ ; & \rho_{el} = 2.5\times 10^{-4} - 10^{-6}\,T + 1.27\times 10^{-9}\,T^2 \\ \kappa = 32 - 8.9\times 10^{-2}\,T + 1.1\times 10^{-4}\,T^2\ ; & \kappa = 0.51 - 6.7\times 10^{-4}\,T + 3.5\times 10^{-6}\,T^2 \\ \alpha = 5.3 - 3.8\times 10^{-2}\,T + 2\times 10^{-4}\,T^2\ ; & \alpha = 1.9\times 10^{2} - 1.1\,T + 2.86\times 10^{-3}\,T^2 \\ & L = \big(68 + 0.407\,T\big)\times 10^3 \end{array} \tag{8}$$

Acknowledgements

This investigation has been developed in the framework of an ongoing research project: **Grant TED2021-129298B-I00**, "Una nueva generación de dispositivos termoeléctricos basado en multicapas semiconductoras magnéticas", funded by **MCIN/AEI Recuperación, Transformación y Resiliencia** and by **EU Next Generation**. The authors want to express their gratitude to the financial support provided.

REFERENCES

[1] D. Castro, L. Goux, G. Hurkx, K. Attenborough, R. Delhougne, J. Lisoni, F. Jedema, M. Zandt, R. Wolters, D. Gravesteijn, M. Verheijen, M. Kaiser, R. Weemaes, and D. Wouters, "Evidence of the thermo-electric thomson effect and influence on the program conditions and cell optimization in phase-change memory cells," in *IEEE International Electron Devices Meeting, Washington DC*, 2007, pp. 315–318.

[2] D. Suh, C. Kim, K. Kim, Y. Kang, T. Lee, Y. Khang, T. Park, Y. Yoon, J. Im, and J. Ihm, "Thermoelectric heating of ge2sb2te5 in phase change memory devices," *Applied Physics Letters*, vol. 96, no. 12, p. 123115, 2012.

[3] A. Faraclas, G. Bakan, L. Adnane, F. Dirisaglik, N. Williams, A. Gokirmak, and H. Silva, "Modeling of thermoelectric effects in phase change memory cell," *IEEE Transactions on Electron Devices*, vol. 61, no. 2, pp. 372–378, 2014.

[4] F. Dirisaglik, G. Bakan, A. Faraclas, A. Gokirmak, and H. Silva, "Numerical modeling of thermoelectric thomson effect in phase change memory bridge structures," *International Journal of High Speed Electronics and Systems*, vol. 23, no. 01n02, p. 1450002, 2014.

[5] C. Ma, J. He, J. Lu, J. Zhu, and Z. Zhu, "Modeling of the temperature profiles and thermoelectric effects in phase change memory cells," *Applied Sciences*, vol. 8, p. 1238, 2018.

[6] A. Sebastian, M. L. Gallo, and E. Eleftheriou, "Computational phase change memory: beyond von neumann computing," *Journal of Physics D: Applied Physics*, vol. 52, no. 44, p. 443002, 2019.

[7] H. Nazeer, H. Bhaskaran, L. Woldering, and L. Abelmann, "Young's modulus and residual stress of gesbte phase-change thin films," *Thin Solid Films*, vol. 592, pp. 69–75, 2015.

[8] J. Perez-Aparicio, R. Palma, and R. Taylor, "Multiphysics and thermodynamic formulations for equilibrium and non-equilibrium interactions: non-linear finite elements applied to multi-coupled active materials," *Archives of Computational Methods in Engineering*, pp. 535–583, 2016.

[9] J. Perez-Aparicio, H. Sosa, and R. Palma, "Numerical investigations of field-defect interactions in piezoelectric ceramics," *International Journal of Solids and Structures*, vol. 44, no. 14-15, pp. 4892–4908, 2007.

[10] R. Palma, J. Pérez-Aparicio, and R. Taylor, "Dissipative finite-element formulation applied to piezoelectric materials with the debye memory," *IEEE/ASME Transactions on Mechatronics*, vol. 23, no. 2, pp. 856–863, 2018.

[11] S. R. Idelsohn, M. A. Storti, and L. A. Crivelli, "Numerical methods in phase-change problems," *Archives of Computational Methods in Engineering*, vol. 1, no. 1, pp. 49–74, 1994.